Engineering with Computers
https://doi.org/10.1007/s00366-022-01765-9

ORIGINAL ARTICLE

A deep learning-based multi-fidelity optimization method for the design of acoustic metasurface

Jinhong Wu[1] · Xingxing Feng[2] · Xuan Cai[2] · Xufeng Huang[1] · Qi Zhou[1]

Received: 8 July 2022 / Accepted: 16 November 2022

Abstract
A desirable acoustic metasurface requires the scattered acoustic field distribution uniform. Neural networks are effective substitutions to mimic the expensive FE simulations in most research. However, the computational cost required to construct a model with only single high-fidelity (HF) simulation data is still unacceptable. This paper presents a deep learning-based multi-fidelity optimization framework to improve the uniformity of the scattered acoustic field distribution. First, a multi-fidelity composite convolutional neural network (MF-CCNN) method is proposed to predict the high-dimensional scattered acoustic field at a lower data cost. The developed MF-CCNN consists of four convolutional subnets. The first part predicts a low-fidelity (LF) output, whose features are then extracted by the second part and concatenated with the inputs to predict the HF result. Two parallel branches are utilized to map the LF features to the HF output. Then, the physical parameters' optimization neural network is proposed to minimize the objective under the prediction of MF-CCNN. The proposed method is compared with other state-of-the-art multi-fidelity networks, and the results demonstrate that MF-CCNN reaches the highest accuracy and the mean absolute error is improved by at least 20%. The variance of the obtained scattered acoustic field after optimization is reduced by 3.62%, and the time cost is only 8% of the genetic algorithm (GA), proving the efficiency and accuracy of the proposed framework.

Keywords Convolutional neural network · Multi-fidelity · Acoustic metasurface · Field prediction · Optimization

1 Introduction

Acoustic metamaterial [1, 2] is a kind of artificial structure material applied in the realm of acoustics. It has become a research hotspot because of its superior ability to manipulate sound waves [3]. With the abnormal reflection and refraction characteristics to sound waves, some special application requirements can be achieved, such as diffuse reflection [4], acoustic focusing [5], acoustic absorption [6], acoustic cloaking [7], and acoustic communication [8]. Traditional metamaterials have drawbacks such as large volume, high manufacturing cost, and narrow bandwidth. To solve the above problems, an artificial structure of acoustic metasurface [9–11] has been proposed, which is a two-dimensional metamaterial designed by analogy with optical metasurface. The acoustic metasurfaces consist of subwavelength microstructure units obeying the generalized Snell's law [12] and can realize manipulation of reflected or refracted waves by applying abrupt phase shifts at the interface.

To achieve acoustic cloaking with uniform reflection waves [13], specific phase gradients of the metasurfaces must be designed. The conventional method needs to execute high-performance numerical simulation models repeatedly to obtain information about the acoustic field and optimize the physical property parameters of the metasurfaces, which turns the optimization process into a high-dimensional, black-box, and time-consuming problem [14–16]. The key to metasurfaces design lies in the rapid prediction of sound field distribution and acoustic performance. Therefore, surrogate models such as the Kriging model are utilized in engineering to replace simulation models to reduce computational and time costs [17]. Nevertheless, these shallow models are less effective in dealing with high-dimensional problems due to their limited representation ability. In recent years, data-driven deep learning methods have been widely

✉ Qi Zhou
qizhou@hust.edu.cn; qizhouhust@gmail.com

[1] School of Aerospace Engineering, Huazhong University of Science and Technology, Wuhan 430074, Hubei, China

[2] Wuhan Second Ship Design and Research Institute, Wuhan 430064, Hubei, China

Published online: 28 November 2022

applied in the realm of field prediction [18–21], which utilize deep neural networks [e.g., convolutional neural network (CNN) and recurrent neural network (RNN)] to learn the representations from high-dimensional data automatically. For instance, Liang et al. [22] developed a neural network scheme for estimating aorta stress distributions, which achieved the mean relative error (MRE) of 0.89% by training on 729 samples. Nie et al. [23] established two different CNN models that take the loads, geometry features, and boundary conditions as inputs and output the stress distribution over the surface of the cantilever beam. The models were trained and evaluated on a dataset containing 120,960 samples, which achieved the MRE of 10.43% and 2.04%, respectively. Guo et al. [24] first utilized CNN to predict the non-uniform steady laminar flow field on a dataset with 10,000 samples, whose computational cost was much lower than the graphics processing unit (GPU) accelerated computational fluid dynamics (CFD) solver. Sekar et al. [25] combined the multilayer perceptron (MLP) and CNN to generate the incompressible laminar flow field around airfoils. Kim et al. [26] and Wu et al. [27] used generative adversarial network (GAN) to predict unsteady flow fields for the first time, which showed that GAN can describe a variety of fluid behaviors and is 700 times faster than CFD solver. Fan et al. [28] proposed mapping from a convex section to distribution with CNN. Donda et al. [29] proposed a 2D CNN network to derive the absorption spectrum responses of metasurface absorbers, which extremely accelerated the design process. Zhao et al. [30] used CNN to explore the relationship between sound pressures and solved the inverse design of metasurfaces. Gao et al. [31] constructed a deep auto-encoder network to predict the peak points and directed the design of the Helmholtz resonator. Liao et al. [32] established a deep neural network surrogate model (DSM) to map the geometric parameters into effective mechanical properties and optimized a given tetra-chiral auxetic with analytical sensitivity analysis successfully.

Indeed, the training effect of neural networks dramatically relies on the quantity and quality of the dataset, which requires meticulously preparing the HF data. The acquisition of HF data is a computationally expensive process, whereas low-fidelity (LF) data is relatively easier to obtain. Nevertheless, only using HF data will suffer from the high cost of simulation analysis, while the model built only with LF data has lower precision. To balance the contradiction between model accuracy and data acquisition cost, scholars have proposed a variety of multi-fidelity modeling methods to fuse data with different precisions effectively [33–35]. Liu and Wang [36] proposed an effective multi-fidelity physical constrained neural network (MF-PCNN), which obtained lower errors on the dataset with much smaller amounts of HF samples than LF compared with the single-fidelity model. Meng et al. [37] constructed a composite neural network to solve the PDE problems. Zhang et al. [38] used CFD simulation data of different grid sizes to establish a neural network model to optimize the shape of the RAE2822 airfoil. The optimization efficiency is greatly improved and the prediction accuracy is comparable to the HF model. Compared with the conventional CFD method, multi-fidelity neural networks have achieved remarkable success in data fusion.

However, the underlying application is yet to be exploited in the field of acoustics. Besides, most of the current research focuses on using massive HF simulation data imposing ingenious architecture to improve the accuracy. Although the MPINNs proposed by Meng et al. [37] can exploit the linear and nonlinear relationships between HF and LF data, the fully connected network architecture is inefficient when dealing with such high-dimensional problems. To address these issues, a deep learning-based multi-fidelity optimization framework of scattered acoustic field uniformity is proposed in this work. Specifically, we introduce a multi-fidelity composite convolutional neural network (MF-CCNN) for scatted acoustic field prediction of acoustic metasurfaces. The physical parameters including density and modulus are the inputs, and the output is the high-dimensional acoustic field matrix. Ideal finite element models (FEMs) of acoustic metasurfaces with different mesh sizes are adopted to generate HF and LF data, respectively. Then, the LF and HF outputs are trained and predicted simultaneously on a dataset consisting of limited HF and massive LF simulation data. A feature extractor and two parallel convolutional subnets are introduced to map the LF output to the HF output. The network without nonlinear activation learns the linear correlation between them, whereas the other part with nonlinear activation extracts the nonlinear correlation. The end-to-end mapping between physical parameters and acoustic fields can be achieved. In addition, the physical parameters' optimization neural network is proposed to be combined with the MF-CCNN to search for the optimal physical parameters of the metasurfaces to minimize the variance of the domain.

The rest of this paper is organized as follows: Sect. 2 introduces the background of acoustic metasurfaces and the corresponding finite element model. In Sect. 3, the overall details of the proposed framework are presented. The MF-CCNN and a brief introduction of two state-of-the-art multi-fidelity neural network methods are presented in Sect. 4. Section 5 provides the model implementation details and the comparison results, followed by the conclusions and future works in Sect. 6.

2 FEM for acoustic field uniformity optimization of acoustic metasurface

This section briefly introduces acoustic metasurface, including the theoretical model and FEM for emulation of the scattered acoustic field. The mathematical model of the acoustic field uniformity optimization problem will be also discussed.

2.1 Acoustic metasurface

The acoustic metasurface is a kind of artificial layered material whose thickness is less than the wavelength of the sound wave. With the extraordinary physical properties such as ultrathin and flexible manipulation of the acoustic wave, it has broad application prospects in wavefront regulation, acoustic imaging, acoustic cloaking, etc. Furthermore, the acoustic metasurface obeys the generalized Snell's law [12], which makes it easy to design the structural parameters to arbitrarily tailor the wave fields.

Generalized Snell's law [39] describes the relationship between incident angle and refraction angle, which can be expressed as

$$n_i \sin\theta_i - n_t \sin\theta_t = \frac{\lambda \mathrm{d}\phi}{2\pi \mathrm{d}x}, \tag{1}$$

where n_i and n_t are the refractive indices of the media through which the incident and refracted waves pass, respectively. θ_i is the incidence angle, θ_t is the refraction angle and λ is the wavelength. $\mathrm{d}\phi/\mathrm{d}x$ is the phase gradient along with the interface, As illustrated in Fig. 1, when the incident wave is vertical to the cross-section, the incidence angle $\theta_i = 0$, hence the refraction angle is

$$\theta_t = \arcsin\left(\frac{\lambda \mathrm{d}\phi}{2\pi n_t \mathrm{d}x}\right), \tag{2}$$

where $\mathrm{d}\phi/\mathrm{d}x$ can be positive or negative. In the case of reflection, $n_i = n_t$, the expression can be rewritten as

$$\sin\left(\theta_i\right) - \sin\left(\theta_r\right) = \frac{\lambda \mathrm{d}\phi}{2\pi n \mathrm{d}x}, \tag{3}$$

where θ_r is the reflection angle, when $\theta_i = 0$, simplification of Eq. (3) yields

$$\theta_r = \arcsin\left(\frac{\lambda \mathrm{d}\phi}{2\pi n \mathrm{d}x}\right). \tag{4}$$

It can be concluded from Eq. (4) that when $\mathrm{d}\phi/\mathrm{d}x \neq 0$, the reflected wave will deviate from the vertical interface by a certain angle even if the wave is incident in a perpendicular cross-section.

In short, an acoustic metasurface can be regarded as a flat structure of subwavelength thickness placed at the interface of two media, at which the sound wave produces phase shifts along a certain direction. With the same angle of incidence, the angle of refraction changes along with $\mathrm{d}\phi/\mathrm{d}x$, allowing arbitrary manipulation of sound waves.

2.2 FEM of acoustic metasurface

In this study, an FE-based acoustic metasurface is utilized to emulate the scattered acoustic distribution, which is then processed as training and testing data. According to Sect. 2.1, the model can be divided into several small elements. Different material properties will be allocated to each element to simulate the ideal metasurfaces. As shown in Fig. 2, the surface is divided into 25 units and the background media is water.

Specifically, the acoustic field is governed by

$$\nabla \cdot \left(-\frac{1}{\rho_c}\left(\nabla p_t - \mathbf{q}_d\right)\right) - \frac{k_{eq}^2 p_t}{\rho_c} = Q_m, \tag{5}$$

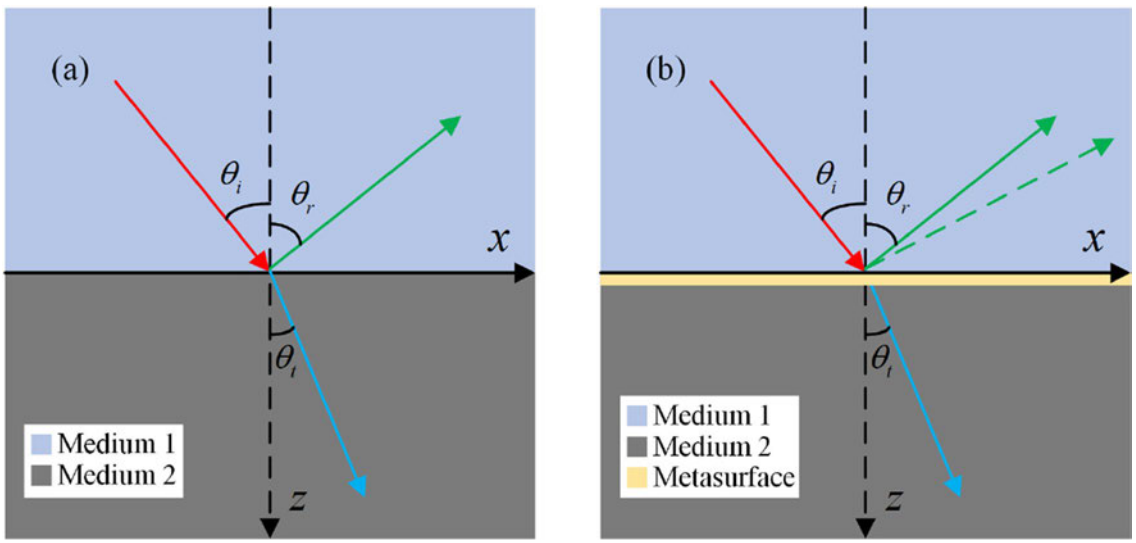

Fig. 1 The generalized Snell's law and acoustic metasurface: **a** without metasurface, **b** with metasurface

where the total pressure (p_t) is the sum of background sound pressure (p_c) and scattered sound pressure (p), k_{eq} is wave number, $\mathbf{q}_d$ represents the dipole domain source, Q_m represents the monopole domain source, and ρ_c is the density of the background media.

There are two initial and boundary condition constraints in this problem as illustrated in Fig. 2. The first one is the background sound pressure distribution, which is a plane wave propagating from the top to the bottom. The other one is the plane wave radiation around the quantity of interest. Besides, the displacement field of the solid structure needs to be calculated when solving for the sound field, which is a complex multi-physics problem consuming expensive computing resources. The above FE-based acoustic metasurface model is constructed in COMSOL Multiphysics 5.4.0 using MATLAB script to carry out batch simulations and data extraction. The average time cost is 38.75 s for each HF sample and 17.5 s for each LF sample, and the computational cost ratio is about 2.25 between them.

2.3 Acoustic field uniformity optimization

It is usually expected that the background incident sound wave is diffused uniformly such that the object (e.g., the Plate in Fig. 2) reflecting the sound wave will not be detected easily. By homogenizing the energy of the scattered acoustic field around the object, acoustic cloaking can be achieved.

The mathematical model of this acoustic field uniformity optimization problem can be described as

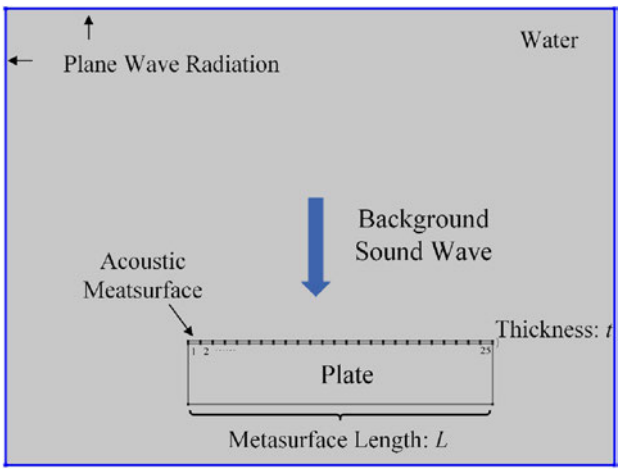

Fig. 2 Acoustic metasurface model

$$\begin{aligned} &\text{Find}: X_\rho, X_E \\ &\text{Objective}: \ \text{minimize var}(P),\ P \in \Omega \\ &\text{Subject to}: \rho_{\min} \le X_\rho^i \le \rho_{\max}\ \forall i = 1, 2, \ldots N \\ &E_{\min} \le X_E^i \le E_{\max}\ \forall i = 1, 2, \ldots N, \end{aligned} \tag{6}$$

where var(P) represents the variance of the scattered acoustic pressure of the domain Ω, X_ρ^i and X_E^i represent the density and Young's modulus of the ith element, $\rho_{\min}$ and $\rho_{\max}$ are the allowable densities range, $E_{\max}$ and $E_{\min}$ are the acceptable maximum and minimum Young's modulus values, respectively. As aforementioned described, the distribution of the scattered acoustic field will be most uniform when it has minimum variance.

3 Deep learning-based optimization framework

The optimization of the scattered acoustic field demands to access the variance corresponding to the design variables, namely, requiring calculating the governing equation to evaluate the acoustic pressure distribution iteratively. However, such computation expensive procedures will turn the optimization process into a time-consuming problem and delay the design cycle. In contrast to executing complex FEM simulation code repeatedly, the deep learning method is proposed to predict the scattered acoustic field directly concerning different inputs. Besides, to accelerate the efficiency, we put forward constructing a neural network model to generate various sets of design variables and optimize the acoustic field through backpropagation.

The proposed deep learning-based optimization framework of scattered acoustic uniformity is illustrated in Fig. 3. This framework is composed of three procedures, i.e., data preparation, multi-fidelity neural network, and physical parameters' optimization.

3.1 Data preparation

To reduce the simulation expenses of the database required to train the neural network model, HF and LF FEMs (e.g., with different mesh sizes) are constructed here. The HF model is more accurate but less calculation effective in contrast to the LF model. It should be noted that the Latin hypercube sampling (LHS) scheme is utilized to cover the acoustic metasurfaces' physical parameters distribution space.

3.2 Multi-fidelity neural network

Once the dataset is constructed, taking the units' physical parameters as input, the neural network surrogate model is trained for predicting the scattered acoustic field. We proposed

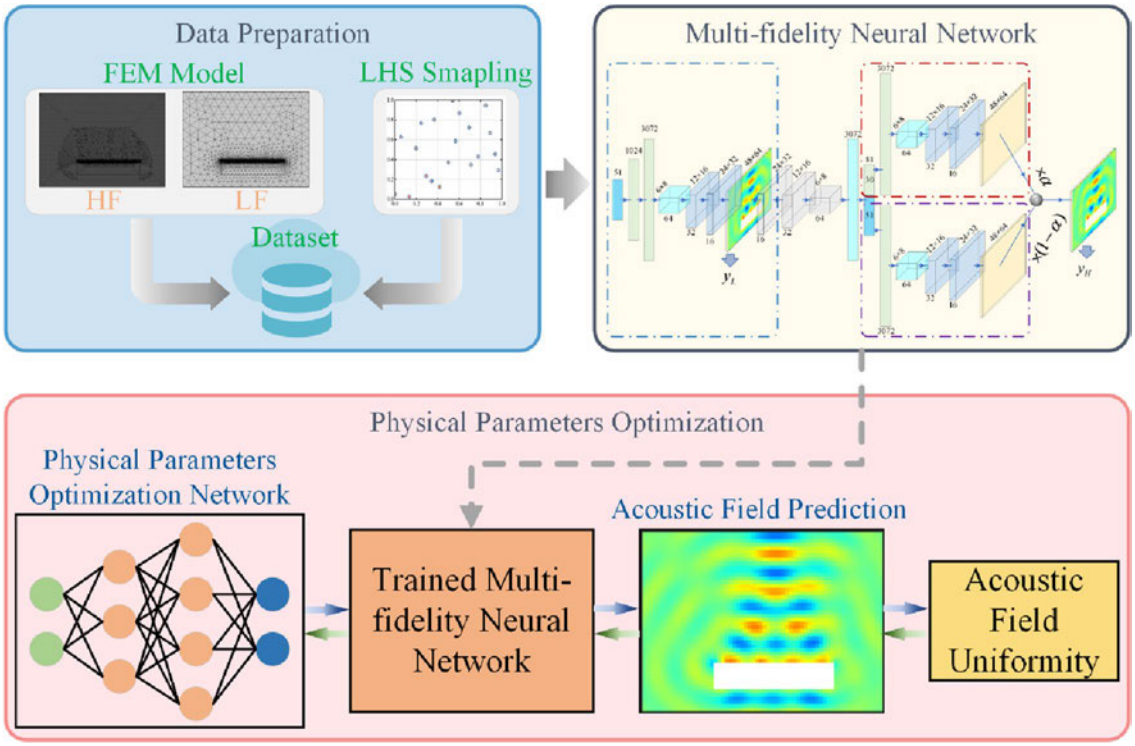

Fig. 3 Optimization framework of scattered acoustic field uniformity

MF-CCNN to exploit the relationship between HF and LF data, which will dramatically improve the accuracy at a lower construction cost.

3.3 Physical parameters' optimization

The physical parameters' optimization is composited of four steps. First, we construct a fully connected neural network model named physical parameters' optimization neural network to represent the densities and Young's modulus of the element (see Fig. 4). The inputs and outputs of the physical parameters network depend on the specific problem. In this paper, e.g., the acoustic metasurface area is divided into 25 elements, so the input layer contains 50 neurons, and the inputs' range from 1 to 50 ($x = [1, \dots 25, \dots, 50]$). The first part $[1, 2, \dots, 25]$ represents the index of densities of these 25 elements, while the last part $[26, 27, \dots, 50]$ represents the index of Young's modulus of these 25 elements. Through some hidden layers, the outputs of the network also contain 50 values, i.e., $[\rho_1, \rho_2, \dots \rho_{25}, E_1, E_2 \dots E_{25}]$. The first part $[\rho_1, \rho_2, \dots \rho_{25}]$ represents the densities of 25 elements and the second part $[E_1, E_2 \dots E_{25}]$ represents Young's modulus of 25 elements. Therefore, the physical parameters' optimization network can be seemed as

$$[\rho_1, \rho_2, \dots \rho_{25}, E_1, E_2 \dots E_{25}] = f(1, \dots 25, \dots, 50), \tag{7}$$

where f represents the network. The aim is to find an optimal group of weights and biases which represents the optimal densities and Young's modulus of 25 elements. The parameters of the physical parameters' optimization network are initialized randomly whose outputs are input into the trained multi-fidelity neural network. The acoustic field is then predicted by a multi-fidelity neural network and the uniformity of the acoustic field is calculated. To minimize the uniformity value of the acoustic field, the loss function is set as

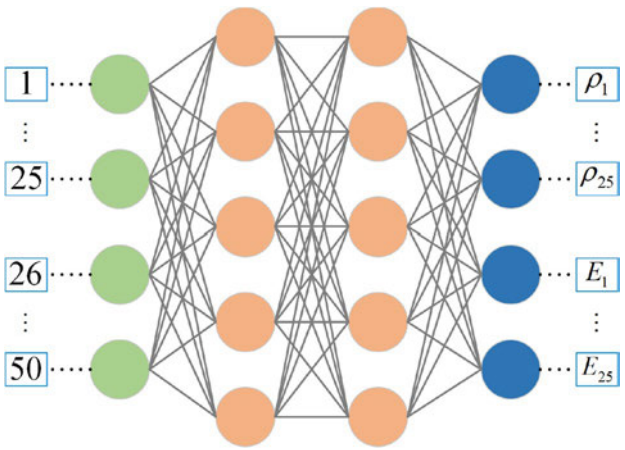

Fig. 4 Architecture of physical parameters' optimization network

$$L = \mathrm{var}(P) = \mathrm{var}(\mathrm{MF}(f(1, 2, \ldots 50))), \tag{8}$$

where var(·) represents the variance and MF represents MF-CCNN. The only trainable parameters are of f and MF-CCNN is frozen. Therefore, the optimization problem has been turned into training the physical parameters' optimization network. Once converging, the outputs of the physical parameters' optimization network are the optimal physical parameters of the acoustic metasurface. It should be emphasized that the inputs and outputs are not fixed according to the optimization problem, and the proposed can be extended to other fields conveniently.

Although heuristic algorithms such as genetic algorithm (GA) are commonly used to solve optimization problems, most of them need to maintain a diversity of the population. GA usually initializes a variety of individuals and evaluates the fitness of every individual and mutates randomly. The such stochastic mutation leads to some unnecessary evaluation, which consumes much time. On the contrary, the proposed physical parameters' optimization network is a gradient-based method, and each iteration is stepped to the gradient orientation. Compared with heuristic algorithms, the physical parameters' optimization network is faster, which can help to cut down on the optimization time.

4 Multi-fidelity neural network for scattered acoustic field prediction

This section describes the proposed MF-CCNN for predicting the scattered acoustic field. As a comparison, we also outline two state-of-the-art neural networks that are available for fusing different fidelities data. They are the multi-fidelity physics-constrained neural network (MF-PCNN) [36] and the bi-fidelity transfer learning with partial network adaptation (BFTL-1) [34].

4.1 Scattered acoustic field prediction using MF-CCNN

How to exploit the relationships between different fidelities data is the critical point of multi-fidelity surrogate modeling. Generally, the most common way is the auto-regressive scheme [40], in which the HF and LF data are expressed as the following relationship:

$$y_{\mathrm{H}} = k(x)y_{\mathrm{L}} + \delta(x), \tag{9}$$

where y_{L} and y_{H} are LF and HF scattered acoustic field data, respectively; the correlation between $\{y_{\mathrm{L}}, y_{\mathrm{H}}\}$ is quantified by the multiplicative correction coefficient $k(x)$, and $\delta(x)$ is the additive scaled function, also called discrepancy function. The model based on Eq. (9) cannot handle complex nonlinear relationships. Whereas there always exist nonlinear correlations between HF and LF data in engineering problems. Therefore, a more generalized formula is

$$y_{\mathrm{H}} = G\left(x, y_{\mathrm{L}}\right), \tag{10}$$

where $G(\cdot)$ is the function mapping LF data and input x to the corresponding HF data. To adaptively find this relationship, $G(\cdot)$ is decomposed into two sectors, thus [37]

$$G = G_{\mathrm{l}} + G_{\mathrm{nl}}, \tag{11}$$

where G_{l} describes the linear correlation and G_{nl} represents the nonlinear correlation, respectively, which is further rewritten as

$$y_{\mathrm{H}} = \alpha G_{\mathrm{l}}\left(x, y_{\mathrm{L}}\right) + (1-\alpha)G_{\mathrm{nl}}\left(x, y_{\mathrm{L}}\right),\ \alpha \in [0, 1], \tag{12}$$

where the hyper-parameter α represents the degree of linear correlation between HF and LF data. To study the Eq. (12) from data, we should construct a neural network to predict LF output $\hat{y}_{\mathrm{L}}$, thus

$$\hat{y}_{\mathrm{H}} = \alpha G_{\mathrm{l}}\left(x, \hat{y}_{\mathrm{L}}\right) + (1-\alpha)G_{\mathrm{nl}}\left(x, \hat{y}_{\mathrm{L}}\right),\ \alpha \in [0, 1]. \tag{13}$$

From Eq. (13), G can be obtained if using two other NNs to fit G_{l} and G_{nl}, respectively. However, studying the relations between high-dimensional matrices $\hat{y}_{\mathrm{L}}$ and $\hat{y}_{\mathrm{H}}$ might cause information redundancy and introduce unnecessary model parameters. We introduce another network ψ to extract the features of $\hat{y}_{\mathrm{L}}$ and rewrite Eq. (13) as

$$\hat{y}_{\mathrm{H}} = \alpha G_{l}\left(x, \psi\left(\hat{y}_{\mathrm{L}}\right)\right) + (1-\alpha)G_{\mathrm{nl}}\left(x, \psi\left(\hat{y}_{\mathrm{L}}\right)\right),\ \alpha \in [0, 1]. \tag{14}$$

Based on this, the architecture of our proposed MF-CCNN for scattered acoustic field prediction is illustrated in Fig. 5. The model is composed of four components: the LF output (θ_{L}), the LF feature extractor (ψ_{L}), the linear (G_{l}), and the nonlinear (G_{nl}) correlation part between the LF output and HF output. Given an input x, θ_{L} will predict the LF result y_{L} that is boxed by blue dashed lines in Fig. 5. The high-dimensional features are then extracted through ψ_{L} and concatenated with the input x. The concatenated vector $\left\{\psi_{\mathrm{L}}\left(\hat{y}_{\mathrm{L}}\right), x\right\}$ is passed to two parallel modules. As shown in Fig. 5, the upper half of the network without activation function is utilized to learn the linear correlation. While the lower half with the activation function is used to learn the nonlinear relationship, and the weighted sum of the two outputs is the final prediction result. Inspired by Nie et al. [23], in which they established a model named SCSNet to predict the stress field of cantilevered structures. SCSNet is an "auto-encoder" like architecture, which extracts the high-dimensional features of the original image through convolutional layers and pooling layers, and then decodes the features concatenated with parameters

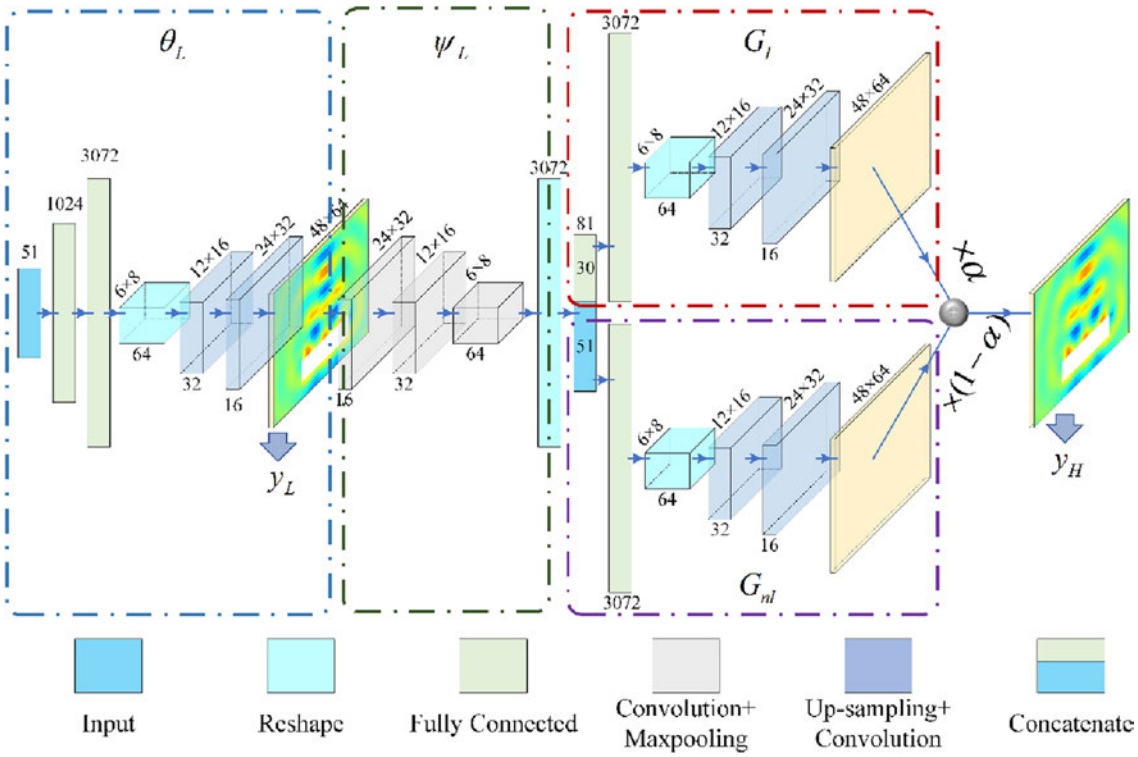

Fig. 5 Architecture of proposed MF-CCNN

through some up-sampling layers and convolutional layers to reconstruct the stress field. Therefore, the architecture of "Fully Connected Layers-Up-sampling Layers-Convolutional Layers" is adapted in this paper to map the high-dimensional vector into the acoustic filed matrix, and the architecture of "Convolutional Layers-Pooling Layers" is used to encode the acoustic filed matrix into high-dimensional vector. The batch normalization layers are adopted to reduce the gradient vanishing problem.

With these basic architectures, θ_{L} utilizes the "Fully Connected Layers-Up-sampling Layers-Convolutional Layers" to map the 51-dimensional physical parameters vector into LF acoustic field matrix. ψ_{L} adopts the "Convolutional Layers-Pooling Layers" to extract the high-dimensional feature of the LF result and then concatenate it with the inputs. G_{l} and G_{nl} both use the "Fully Connected Layers-Up-sampling Layers-Convolutional Layers" to reconstruct the final matrix. G_{l} contains no nonlinear activation function to learn the linear relationship between HF and LF data, whereas G_{nl} learns the nonlinear relationship.

For a neuron, its output can be expressed as

$$y_j = \sigma\left(\sum\left(\omega_i x_i + b_j\right)\right), \tag{15}$$

where x_i is the input of the neurons in the ith layer; ω_i is the weight between the ith layer and jth layer neurons, and σ is the activation function that makes the layers nonlinear. Therefore, G_{l} will only be trained to learn the linear correlation between $\left\{\psi_{\mathrm{L}}\left(\hat{y}_{\mathrm{L}}\right), x\right\}$ and $\hat{y}_{\mathrm{H}}$, while G_{nl} will only be used to fix the nonlinear function. In this work, we mainly study the mapping of physical parameters to the acoustic field, thus the model input is the parameter vector, and the output is the field matrix.

Specifically, the output $\hat{y}_{\mathrm{L}}$ of θ_{L} should be as close as possible to the real LF sample, and the predicted value $\hat{y}_{\mathrm{H}}$ should also approximate the corresponding real HF sample. These yield two types of error, the LF error term, and the HF error term, which need to be considered. We combine them and rewrite the loss function as

$$L = \gamma\left\|\hat{y}_i^{\mathrm{L}} - y_{\mathrm{L}}\right\| + (1-\gamma)\left\|\hat{y}_i^{\mathrm{H}} - y_{\mathrm{H}}\right\|, \tag{16}$$

where $\hat{y}_i^{\mathrm{L}}$ and $\hat{y}_i^{\mathrm{H}}$ represent the real LF and HF data, respectively; γ is the corresponding weight coefficient; $(1-\gamma)$ is the weight coefficient of the HF output error term; $\|\cdot\|$ represents the Euclidean distance.

In the multi-fidelity surrogate modeling problems, it is commonly assumed that there are massive LF samples but limited HF data. However, MF-CCNN needs to use both LF and corresponding HF data during the training period. To solve this problem, referring to Zhou et al. [33], the lacking portion of the HF data is filled with corresponding LF data, which is called "pseudo" HF data, as shown in Fig. 6. To distinguish these data, each sample point is

assigned a different weight, thus the loss function can be rewritten as

$$L = \beta_i^{\mathrm{L}} \gamma \left\| \hat{y}_i^{\mathrm{L}} - y_{\mathrm{L}} \right\| + \beta_i^{\mathrm{H}} (1-\gamma) \left\| \hat{y}_i^{\mathrm{H}} - y_{\mathrm{H}} \right\|, \tag{17}$$

where β is the weight coefficient of each sample point. For "pseudo" HF data, β is set close to 0, which means that the former won't have effects on the parameter updating of G_{l} and G_{nl}.

4.2 Scattered acoustic field prediction using MF-PCNN

This section briefly introduces the basic principles of MF-PCNN, more details are available in Ref. [36]. Here the physics-constrained part is discarded cause we only consider a purely data-driven method. The scheme of MF-PCNN is analogous to the widely used multi-fidelity Gaussian process modeling. As shown in Fig. 7, The MF-PCNN is combined with an LF neural network (LF-PCNN), an HF neural network (HF-PCNN), and a discrepancy artificial neural network (DANN).

The LF-PCNN and HF-PCNN are trained with LF and HF data, respectively. Whereas the DANN is trained with the discrepancy between the prediction results of HF-PCNN and LF-PCNN. The prediction results of LF-PCNN and DF-PCNN are added to obtain the final prediction result.

4.3 Scattered acoustic field prediction using BFTL-1

Transfer learning is one of the commonly utilized methods in deep learning, which can effectively reduce the cost of acquiring data by reapplying the model trained on one task for another task. At present, some scholars have studied the feasibility of using the transfer learning method to fuse multi-fidelity data. Generally, the neural network can learn the high-dimensional features of the data under its powerful feature extraction ability. The model is trained on the LF data to map from input to output first. Then the parameters of the LF network can be fine-tuned using HF data. Here, we adopt the BFTL-1 model proposed by De et al. [34]

5 Algorithm details and discussion

We first emulate HF and LF data based on the finite element model of the acoustic metasurface in this section. Then the obtained data is processed into training and testing datasets. To demonstrate the effectiveness of the proposed multi-fidelity approach, MF-CCNN, MF-PCNN, and BFTL-1 models are also compared with neural networks only trained with single-fidelity data under a different number of samples. Finally, we combine the physical parameters' optimization neural network with the well-trained MF-CCNN to obtain the approximately optimal physical parameters and compare it with the GA.

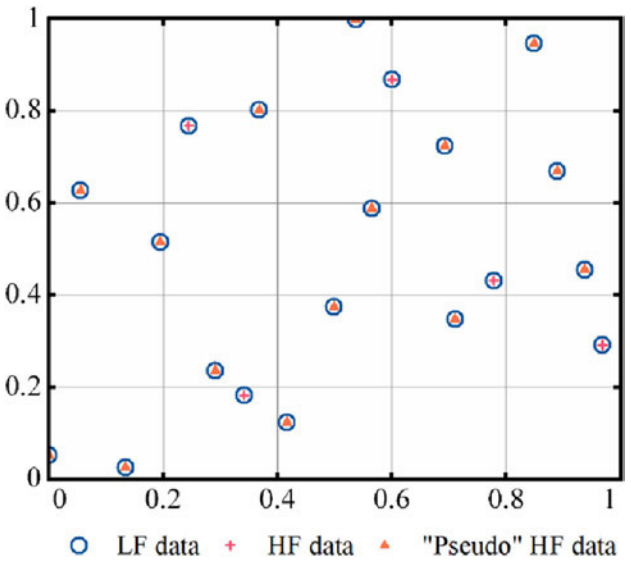

Fig. 6 Handling strategies for mismatched data in MF-CCNN

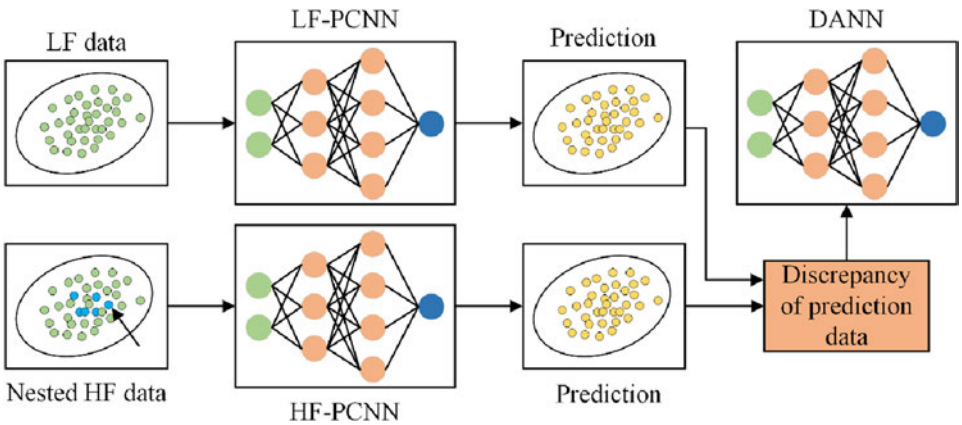

Fig. 7 Algorithm diagram of the MF-PCNN

5.1 Dataset generation and processing

In this study, one of the critical points is the generation of data with different fidelities. There are different categories of fidelities because HF and LF are relative, such as meshes of varying grid scales, different finite element solvers, iteration times, etc. Here, the LF model is obtained by magnifying the mesh size. Figure 8a, b shows the meshes of the HF and LF models, respectively. The simulation frequency studied here is 500 Hz. The dimensions of the plate are 10×2 m, and the thickness of the metasurface is 0.08 m. The metasurface domain of the HF and LF models are divided into 6254 triangular meshes whose maximum side length is 0.02 m, and the other parts are divided into triangular meshes with a maximum length of 0.1 and 1.5 m, respectively. The total elements for these two models are 97,408 and 20,469 respectively. The mesh convergence analysis for finite elements is shown in Fig. 9, indicating that the HF model has reached convergence. The computational cost ratio of an HF sample and an LF sample is about 2.25.

The Young's modulus of the plate is 1.08×10^9 Pa, the Poisson's ratio is 0.34, and the density is 4500 kg/m^3. While the density of the metasurface elements varies from 333.33 to 2000 kg/m^3, the modulus ranges from 7.5×10^8 to 1.35×10^9 Pa. Specifically, the material properties of each unit are randomly selected within the range.

The Multifrontal Massively Parallel Sparse (MUMPS) frequency-domain solver is utilized to simulate a randomly generated metasurface, whose parameter definitions are shown in Table. 1. The distributions of the scattered acoustic field without and with metasurface are shown in Fig. 10. It can be concluded that the application of metasurface has a certain influence on the acoustic wave.

To generate the regular domain data required by CNNs, the regular grid points are extracted by interpolation from the unstructured finite element meshes, as illustrated in Fig. 11. Notably, the larger the dimension of the extracted grid matrix, the smaller the discrepancy between the obtained and the original field. A suitable dimension 48×64 is selected here, which could approximate the original acoustic field. As shown in Fig. 11, the distribution trend of extracted HF and LF data is similar to that of the real field, with only less accuracy loss.

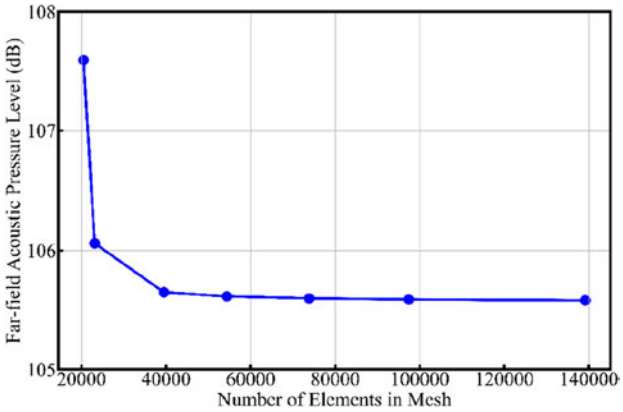

Fig. 9 Finite-element analysis convergence

The absolute errors of HF and LF data are plotted in Fig. 12. It can be seen that there are obvious discrepancies between HF and LF data and nonlinear correlations. While the Pearson correlation coefficients of HF and LF data are above 0.8 as shown in Fig. 13a. Since there are 3072 points in total, to make it clearer, the scatter figure belonging to the point with the lowest value, which is in the top left of the matrix is plotted. As can be seen from Fig. 13b, there is a strong linear relationship between HF and LF data, and a slight nonlinear relationship. The remained points' scatter plots had also been examined, and all of them demonstrate

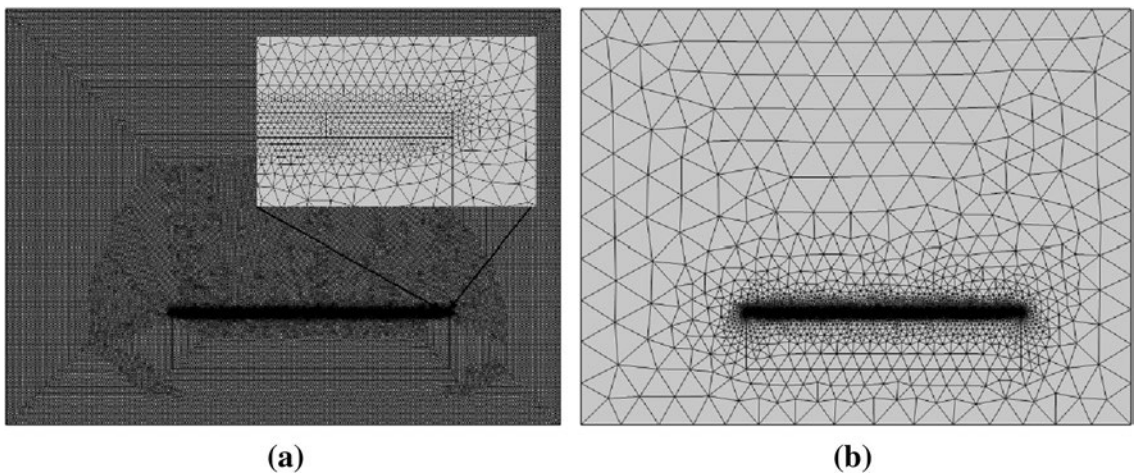

Fig. 8 Metasurface FEM mesh: **a** HF model, **b** LF model

Table 1 The material parameters of metasurface

Element number	Density/(kg/m^3)	Modulus/(MPa)	Element number	Density/(kg/m^3)	Modulus/(MPa)
1	1.86	6.98	14	1.27	13.11
2	1.01	11.19	15	1.97	13.38
3	1.58	2.54	16	1.93	11.08
4	0.67	10.50	17	0.36	6.52
5	0.54	5.76	18	1.45	4.35
6	0.85	7.43	19	0.67	8.99
7	0.74	8.80	20	0.89	10.17
8	0.45	9.60	21	1.80	1.89
9	1.80	11.12	22	1.06	3.59
10	1.26	4.89	23	1.61	4.48
11	1.54	3.34	24	1.86	2.48
12	1.69	10.86	25	0.82	7.16
13	1.15	10.36			

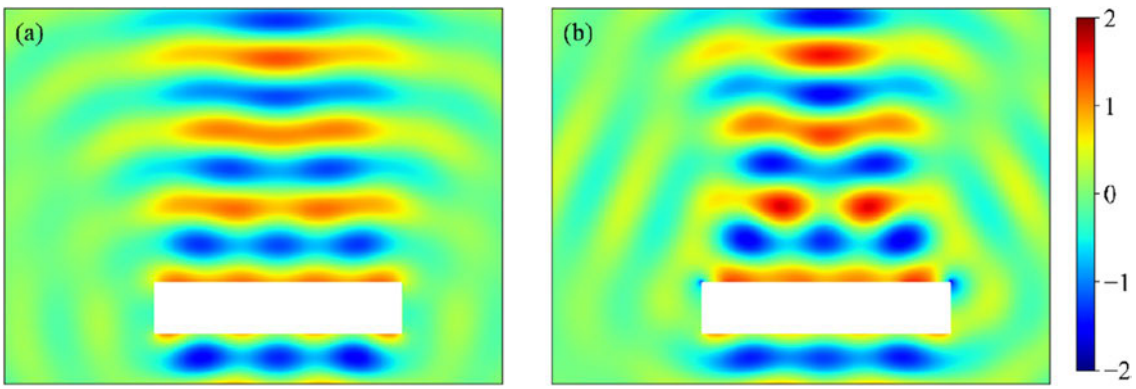

Fig. 10 Scattered sound pressure level field. **a** Without metasurface, **b** with metasurface

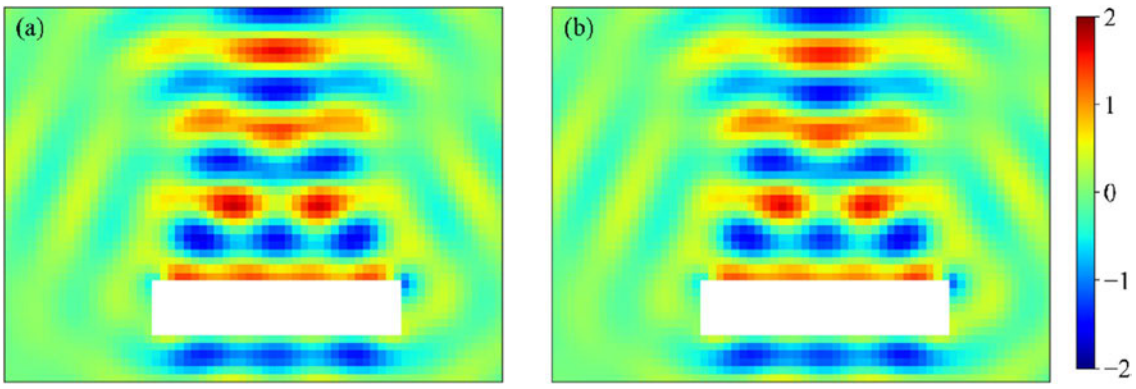

Fig. 11 Extracted scattered acoustic field. **a** LF, **b** HF

this conclusion. A test of significance of the Pearson's coefficient also needs to be executed to further check the reliability of the above result. Cause the t-test is used for Pearson's coefficient, first, whether the data satisfy the precondition is checked. The preconditions are as follows:

(1) The overall distribution is normal, which is also a precondition of many hypothesis tests. To do so, the histograms of both HF data and LF data are plotted, and Fig. 13c, d illustrates which of the point in the top left corner. Two probability density curves satisfy the normal distribution.

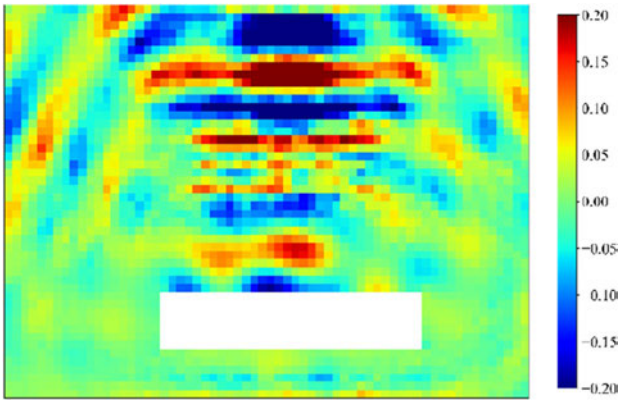

Fig. 12 HF and LF data error distribution

(2) The value of data should not contain noise, which is also satisfied in the dataset.

(3) Every set of samples is independent and identically distributed. The LHS used here satisfies this requirement.

Pearson's coefficient could be constructed as a statistical parameter t, which is formulated as

$$t = r \cdot \sqrt{\frac{n-2}{1-r^2}}, \tag{18}$$

where n is the sample number and r is Pearson's coefficient. t obeys a t-distribution with freedom of two. The null hypothesis is that HF and LF data have no correlation, and the alternative hypothesis is that they do have an apparent correlation. Under a confidence level of 99%, the p-value is 0.01. The maximum p-value of the results is 2.24×10^{-134}, which is much less than 0.01, indicating that the hypothesis that LF data can provide certain trend information for HF data is reasonable. In this paper, the LHS scheme is utilized to generate 500 samples within the parameters range to ensure uniformity in the design space. Then each sample is simulated to generate both HF and LF data.

The 51-dimensional vector representing the density and modulus of the 25 elements and the simulation frequency is input to the neural network, which is also standardized by

$$\sigma_{ij} = \frac{\sigma_{ij} - \text{mean}_j(\sigma_{ij})}{\text{std}_j(\sigma_{ij})}, \; i = 1, \ldots, 500; j = 1, \ldots, 50, \tag{19}$$

where $\text{mean}_j(\sigma_{ij})$ is the average value of the jth material property of 500 samples, and $\text{std}_j(\sigma_{ij})$ is the standard deviation.

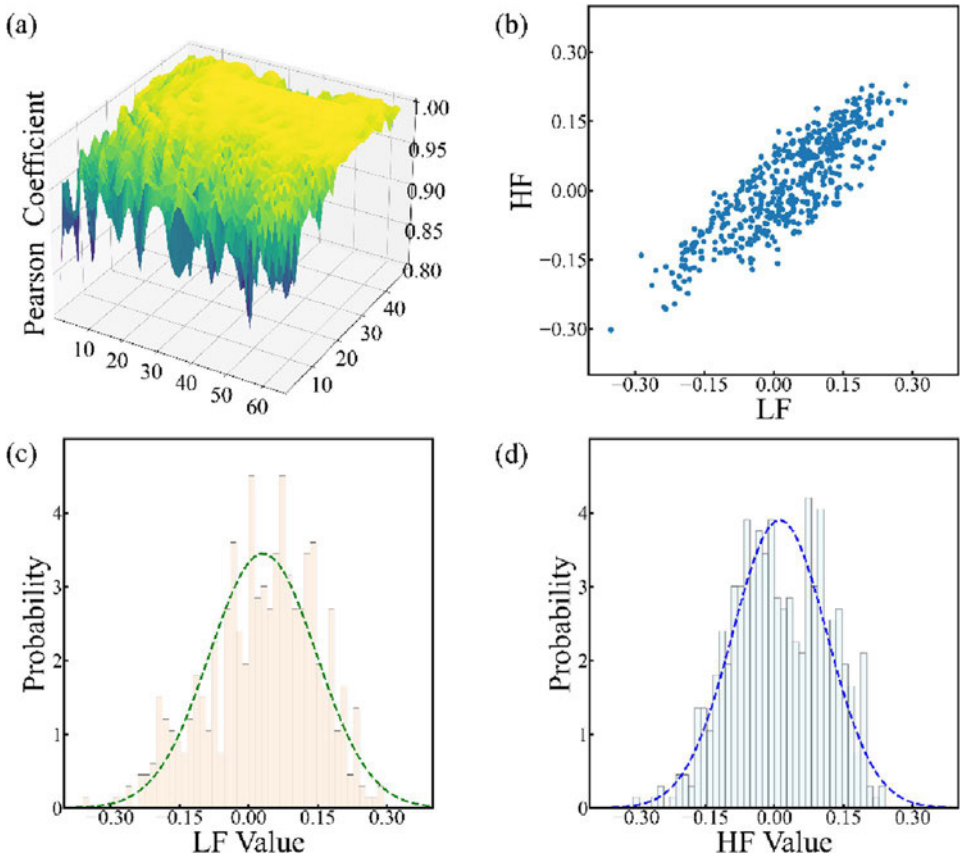

Fig. 13 **a** Pearson correlation coefficient of HF and LF data at each coordinate point. **b** Scatter plot between HF and LF data of the point in the top left of the matrix. **c** Probability density distribution of LF data. **d** Probability density distribution of HF data

5.2 Performance of MF-CCNN

5.2.1 Implementation details of MF-CCNN

As illustrated in Fig. 5, the 51-dimensional input vector is converted into a 3,072-dimensional vector through two fully connected layers, which is then reshaped into a $64 \times 6 \times 8$ feature map. After three up-sampling and convolution layers, the feature map size is 48×64 (i.e., y_L). To obtain accordant features between HF and LF data in MF-CCNN, the convolution kernel size and stride of each convolutional layer are set to 3 and 1, respectively. Then, the features of the LF output are extracted through three convolution and pooling layers, obtaining a $64 \times 6 \times 8$ feature map. The feature map is then compressed into a 30-dimensional feature vector through a fully connected layer, and spliced into an 81-dimensional vector with the input. The last two branches consisted of fully connected, up-sampling, convolution layers, and the feature map size is 3072, $64 \times 6 \times 8$, $32 \times 12 \times 16$, $16 \times 24 \times 32$, 48×64. Batch normalization is adopted after each layer and the activation function is LeakyReLU ($\alpha = 0.1$). The final two feature maps are weighted and added element-wise to obtain HF prediction.

Since the relationship between HF and LF data is unknown here, the value of hyper-parameters α and γ cannot be determined. α determines the linear and nonlinear correlation between HF and LF data, and γ determines the weights of HF loss and LF loss. If α is not selected properly, it will be hard for G_{nl} to learn the correct nonlinear relationship between HF and LF data. If γ is not selected properly, the network will tend to predict the LF result more accurately and neglect the HF result, and vice versa. To be exact, the model could correctly learn the linear and nonlinear relationship of them, which makes the prediction accuracy the highest. Therefore, we can set α and γ as two parameters which tuned by the network itself. But in practice, it is found that this method will make the loss function curve unstable and the model difficult to converge. Besides, the results obtained from each training process are quite diverse. For the sake of acquiring suitable α, the following methods are introduced.

Design the orthogonal experiment, which α and γ is divided into five levels: 0, 0.2, 0.4, 0.6, and 0.8. In general, it is assumed that there is only a small number of HF data, whereas massive LF data is available. Therefore, 450 LF and the nested 90 HF randomly selected samples are set as the training samples. The number ratio of the training set and validation set is 9:1. The other 50 HF samples compose the testing set. The mean relative error (MRE) is used as the evaluation metric, and each parameter is trained three times to obtain the best result, as shown in Table. 2. The mean main effect diagram is shown in Fig. 14. It can be seen that MRE reaches the smallest when $\alpha = 0.2$ and $\gamma = 0.8$.

Table 2 Orthogonal experiment results

α	MRE (%)				
	$\gamma = 0$	$\gamma = 0.2$	$\gamma = 0.4$	$\gamma = 0.6$	$\gamma = 0.8$
0	23.46	23.70	23.30	23.25	23.00
0.2	24.33	24.22	23.51	22.57	23.89
0.4	24.37	24.56	23.59	23.69	23.29
0.6	26.13	23.81	22.59	23.15	22.99
0.8	25.21	23.33	23.05	22.43	22.70

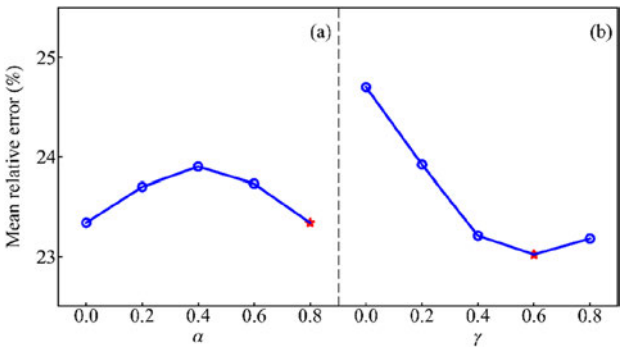

Fig. 14 Mean effect diagram

To ensure the best accuracy of this model, it is trained to converge with the initial $\alpha = 0.2$, and then update α as a trainable parameter with a lower learning rate. The α after training is selected as the final value. The other hyper-parameters are set as follows: the batch size is set as 8; the Adam optimizer is utilized; the initial value of the dynamic learning rate is set to be 0.01 and reduced to 0.5 times when the error does not decrease for 10 iterations. The maximum number of iterations is 500. The best result is saved after each epoch, and the early-stopping strategy is also used. β is used to distinguish the HF and "pseudo" HF data. Therefore, the value of β is not as important to the MF-CCNN as α and γ. For "pseudo" HF data, it is set as close to zero to not make it to disturb the training process. For HF data, it is set a little bigger than one to make the network concentrate more on HF data whose amount is much less than LF data. A value slightly less than one is set for LF data to balance the importance of HF and LF data. As for the hyper-parameter β, it is set to be 0.5 for LF data and 2 for the HF data, while the "pseudo" HF's is set to 1×10^{-5}.

5.2.2 Training details of other methods

As described in Sect. 4, the MF-PCNN consists of LF-PCNN, HF-PCNN, and DANN, whose network architectures are the same as θ_L part of MF-CCNN. The other training strategies are consistent with MF-CCNN except for the batch size (i.e., 2) and the initial learning rate (i.e., 0.005). LF-PCNN is trained

with 450 LF and HF-PCNN is trained with 90 HF data first, and then the trained LF-CNN and HF-CNN are used to predict the output $\hat{y}_{\mathrm{L}}$ and $\hat{y}_{\mathrm{H}}$ of 450 samples, respectively. The DANN is trained with the discrepancy between $\hat{y}_{\mathrm{L}}$ and $\hat{y}_{\mathrm{H}}$. We can get the final output of MF-PCNN by simply adding the LF-PCNN and DANN predictions.

The architecture and hyper-parameters of BFTL-1 are identified with the MF-PCNN. 450 LF samples are utilized to train the network first, and then fine-tuning the weights and biases with the learning rate of 5×10^{-4} by 90 HF samples. In addition, the single-fidelity neural network is also trained with the same architecture, datasets, and hyper-parameters.

5.2.3 Scattered acoustic field prediction result discussion

To compare the performance of the five models fairly, each model is trained three times in the same training environment (i7-9700 K, RTX 2080, PyTorch 1.9.0) and the average results are recorded. Mean absolute error (MAE), mean max absolute error (MMAE), and relative error (RE) are utilized as the evaluation metrics, which are given by

$$\mathrm{MAE} = \frac{1}{N_{\mathrm{samples}}} \sum_{i=1}^{N_{\mathrm{samples}}} \mathrm{mean}\left(\left|y_i - \hat{y}_i\right|\right) \tag{20}$$

$$\mathrm{MMAE} = \frac{1}{N_{\mathrm{samples}}} \sum_{i=1}^{N_{\mathrm{samples}}} \max\left|y_i - \hat{y}_i\right| \tag{21}$$

$$\mathrm{RE} = \frac{\left\|y_i - \hat{y}_i\right\|}{\left\|y_i\right\|}, \tag{22}$$

where $N_{sampels}$ represents the number of testing samples; $|\cdot|$ is the absolute error and $\|\cdot\|$ is the L_2 norm, i.e., Euclidean distance; y_i and $\hat{y}_i$ are the ground truth and predicted acoustic field of the ith testing sample.

Three randomly selected samples from the testing data and the real acoustic field and predicted results of different models are shown in Figs. 15, 16 and 17. It is readily observed that the prediction results of the five models are consistent with the real acoustic field distribution, which reflects the broad application prospects of the data-driven deep learning method of sound field prediction. The deviation of HF-CNN is the largest, and the discrepancy is particularly obvious in the area near the plate. The prediction result of LF-CNN deviates greatly from the ground truth as well. On the contrary, MF-CCNN, MF-PCNN, and BFTL-1 can capture more details of the image. The outputs of MF-PCNN and BFTL-1 are similar, but there are still large discrepancies in some regions where the gradients vary sharply. The prediction precision of MF-CCNN is the best, whose result is closer to the real data even in the area near the plate. Similar conclusions can also be generalized from Figs. 16 and 17. The prediction result of HF-CNN remains almost unchanged in the three samples, indicating the poor generalization ability of HF-CNN.

Figures 18, 19 and 20 plot the error diagrams between the predictions and the ground truth of the three samples. The

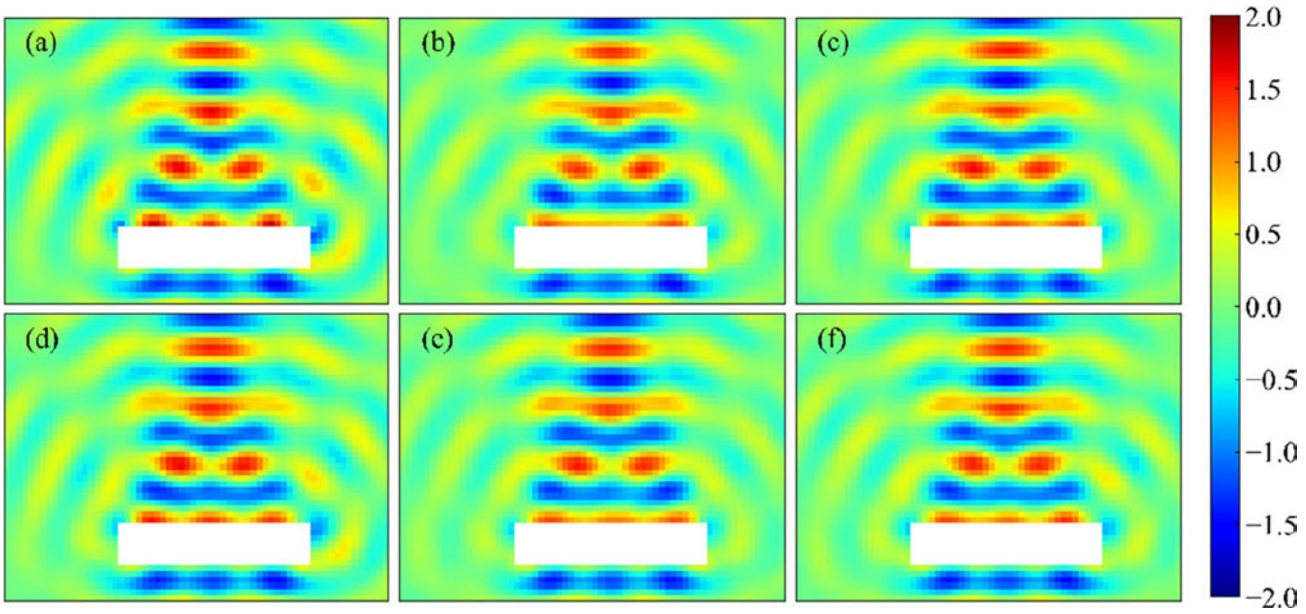

Fig. 15 Comparison between different model predictions (sample 1) **a** ground truth, **b** HF-CNN, **c** LF-CNN, **d** MF-CCNN, **e** MF-PCNN, **f** BFTL-1

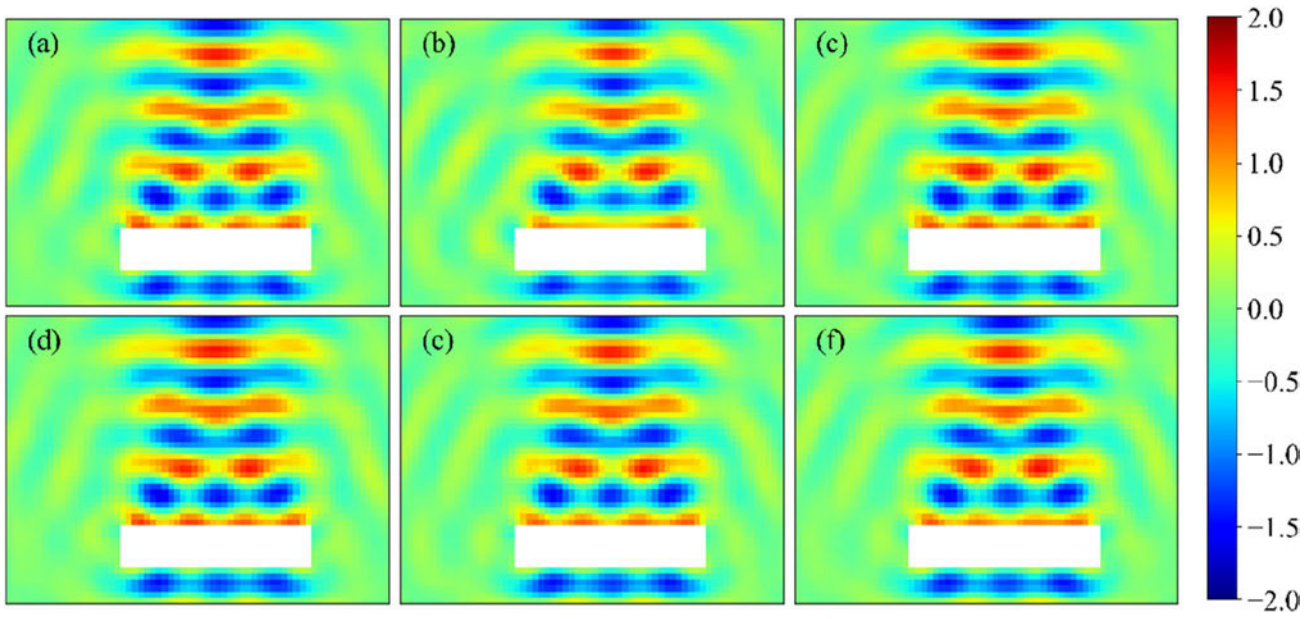

Fig. 16 Comparison between different model predictions (sample 2) **a** ground truth, **b** HF-CNN, **c** LF-CNN, **d** MF-CCNN, **e** MF-PCNN, **f** BFTL-1

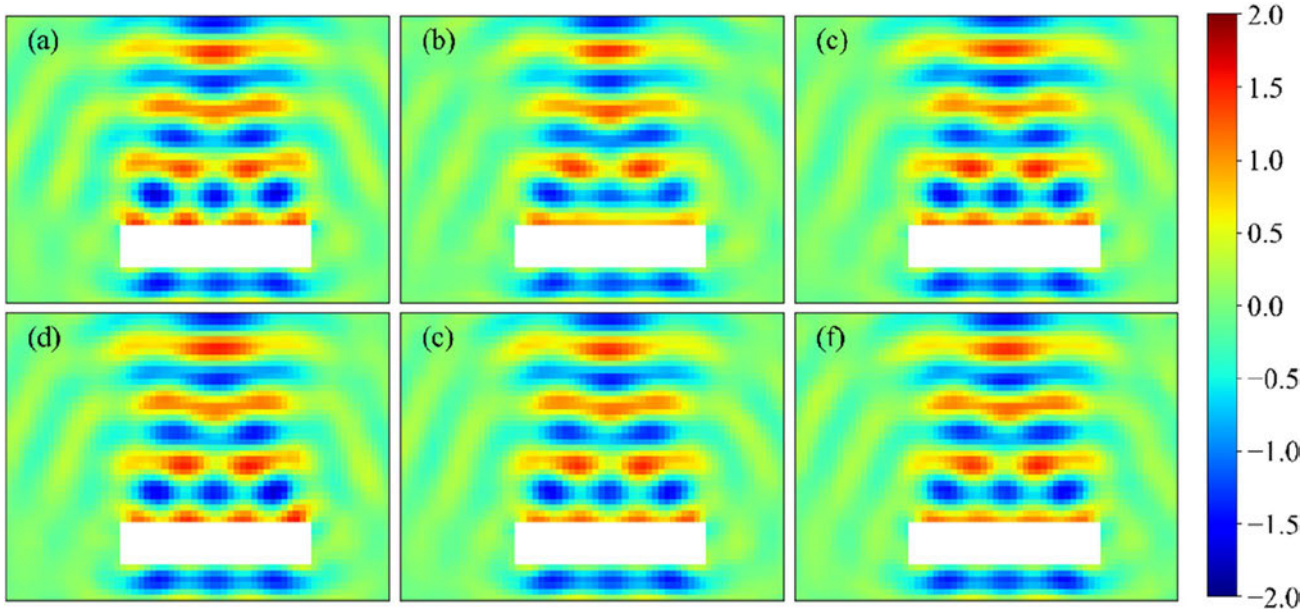

Fig. 17 Comparison between different model predictions (sample 3): **a** ground truth, **b** HF-CNN, **c** LF-CNN, **d** MF-CCNN, **e** MF-PCNN, **f** BFTL-1

errors of HF-CNN are the largest, whereas the discrepancies of MF-CCNN are the smallest among them. It is worth noting that all the error distributions are spokewise and becoming significantly larger where the gradients change sharply, indicating that the prediction performance of the model for severe numerical fluctuations needs to be improved. The probability density function (PDF) of absolute errors of five model predictions (sample 1) is shown in Fig. 21. It can be concluded that the MF-CCNN yields the smallest absolute errors among them, whereas the absolute errors of HF-CNN are the highest. Most of the absolute errors vary from 0.05 to 0.1.

To quantify the comparison, we calculate the MAE, MMAE, and RE of each model, as shown in Table 3. The

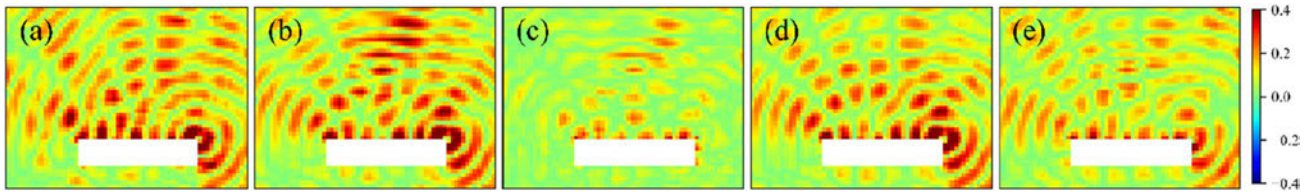

Fig. 18 Absolute errors of different models (sample1): **a** HF-CNN, **b** LF-CNN, **c** MF-CCNN, **d** MF-PCNN, **e** BFTL-1

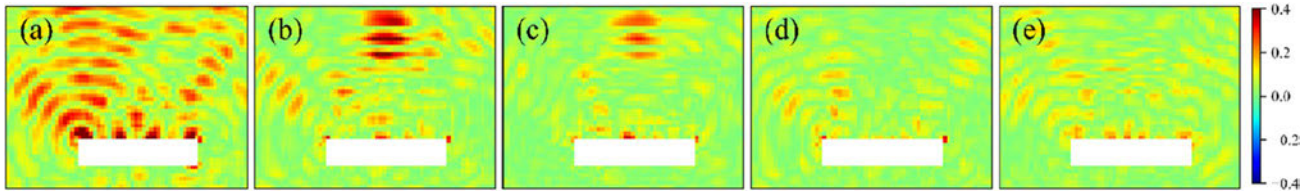

Fig. 19 Absolute errors of different models (sample1): **a** HF-CNN, **b** LF-CNN, **c** MF-CCNN, **d** MF-PCNN, **e** BFTL-1

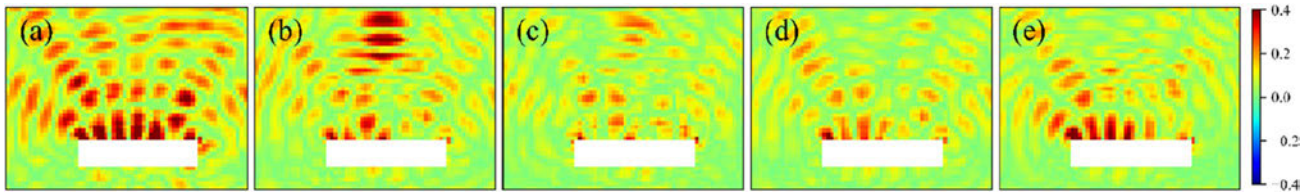

Fig. 20 Absolute errors of different models (sample1): **a** HF-CNN, **b** LF-CNN, **c** MF-CCNN, **d** MF-PCNN, **e** BFTL-1

bold value indicates that it is the best value in this column. In general, The MF-CCNN achieves the smallest MAE, MMAE, and RE among the five models, indicating that the prediction results of MF-CCNN are the closest to the real data. The evaluation metrics of HF-CNN are the worst, indicating that only using limited HF data cannot obtain a model with high accuracy and excellent generalization ability. The MAE, MMAE, and RE of LF-CNN are all better than HF-CNN. Because massive data samples could reduce the error and improve the generalization ability of the neural network. Therefore, improving the data quantity and quality is particularly important for deep learning models. Compared with MF-PCNN and BFTL-1, MF-CCNN can better learn the linear and nonlinear relationship between HF and LF data, thereby improving the accuracy of the neural network.

5.2.4 Effect of the LF and HF samples number ratio

This section will evaluate the effect of the LF and HF sample number ratio γ on different methods. A series of experiments are conducted using 450 LF samples and selecting the γ value of 2, 3, 4, 5, 6, 7, 8, 9, 10, and 15. Each model is trained three times and estimated with the average MRE.

Table 4 and Fig. 22 show the MRE of each model when the number of HF samples varies. The error of HF-CNN is still far greater than that of other methods with the HF data size gradually increasing. The neural network model integrating HF and LF data can dramatically improve the prediction precision. The MF-CCNN achieves the best results, whose precision is ahead of MF-PCNN and BFTL-1 when the sample size ratio is lower than 8. The error of MF-PCNN and BFTL-1 fluctuates when the sample number increases, which proves that MF-CCNN can utilize the correlation between different fidelities data more effectively and has a better stability. According to the previous analysis, these two methods need to learn complex nonlinear functions instead of learning linear and nonlinear relationships between the HF and LF data.

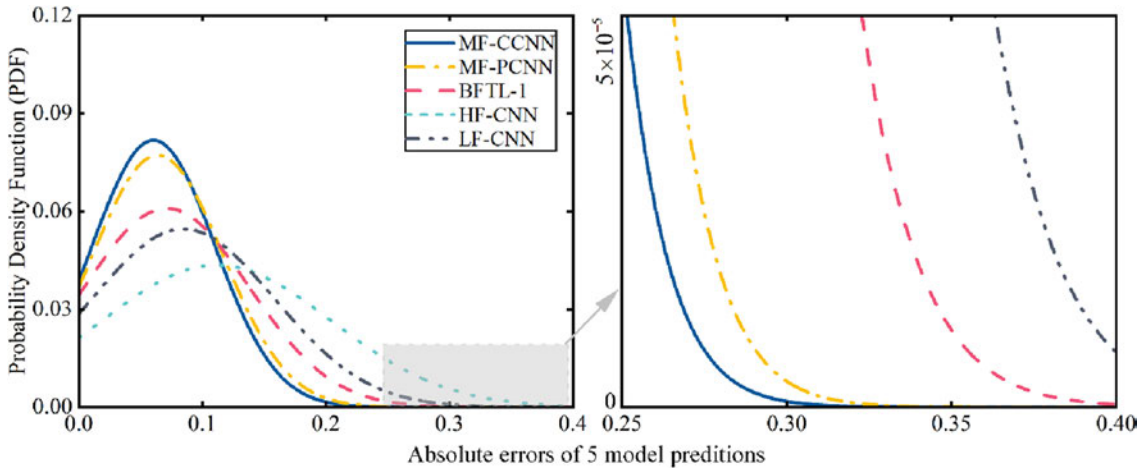

Fig. 21 PDF of absolute errors of 5 model predictions

Table 3 Comparison results of different models for acoustic field prediction

Model	MAE	MMAE	RE (%)		
			Mean	Max	Min
MF-CCNN	**0.0794**	**0.5548**	**20.55**	**36.20**	11.73
MF-PCNN	0.0980	0.5799	21.33	38.38	**11.48**
BFTL-1	0.0859	0.5770	21.52	41.78	11.73
LF-CNN	0.1005	0.6315	25.81	41.26	17.19
HF-CNN	0.1253	0.7614	31.55	55.42	19.53

Table 4 The MRE with various ratios of LF and HF samples sizes

γ	MF-CCNN	MF-PCNN	BFTL-1	HF-CNN
2	18.20	21.21	21.58	24.49
3	18.95	21.66	21.58	25.84
4	19.87	21.20	21.87	26.88
5	20.55	21.33	21.52	31.55
6	20.42	21.57	21.33	32.00
7	21.48	21.76	21.53	32.21
8	20.65	22.20	21.78	33.25
9	21.83	21.99	21.86	41.17
10	21.41	22.04	21.78	40.00
15	23.71	22.53	21.93	71.26

5.3 Deep learning-based acoustic field uniformity optimization

5.3.1 Implementation of physical parameters' optimization neural network

A fully connected neural network architecture model with three hidden layers and one hundred neurons is constructed

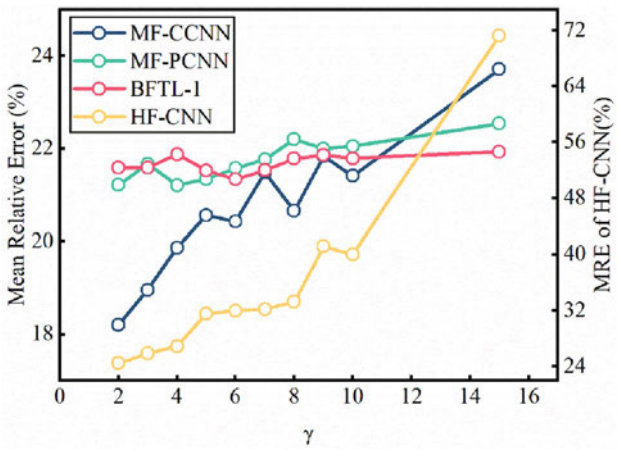

Fig. 22 The MRE with the various ratio of LF and HF sample sizes

to generate a different combination of the units' physical parameters. As described in Sect. 2.3, there are 50 design variables including 25 units' densities and Young's modulus. The input is a fixed integer sequence ranging from 1 to 50, representing the index of each parameter. The output layer consists of 50 neurons with Sigmoid activation to predict the scaling factor between the maximum and minimum allowance values.

The generated physical parameters concatenated with the frequency value are then input into the well-trained MF-CCNN to predict the scattered acoustic field, whose variance is then extracted. To minimize the obtained variance, parameters of physical parameters' optimization neural network will be upgraded through backpropagation.

5.3.2 Result of acoustic field uniformity optimization

We use another 9000 LF samples and 4500 HF samples to retrain the MF-CCNN to obtain a model with better generalization capability, and the MAE is only 0.041 evaluated on the testing dataset with 1000 samples. Based on the trained MF-CCNN, the approximately optimal physical parameters are attained by the physical parameters' optimization neural network through 2000 iterations, costing only 20.03 s.

The comparison between the obtained FEM simulation and MF-CCNN prediction is shown in Table 5 and Fig. 23. The high similarity between the interpolation prediction result of MF-CCNN and the ground truth proves the great generalization ability. The variance is 3.62% lower than the minimum value of these 10,000 samples and the relative error between MF-CCNN prediction and FEM simulation is only 3.71%. which demonstrates that the proposed deep learning-based multi-fidelity optimization framework can realize accurate and rapid optimization of acoustic metasurface scattered field uniformity. We also compare it with the GA optimization method, i.e., replace the physical parameters' optimization neural network with GA. The population size is 3000 and the number of iterations is 500. The result of the proposed physical parameters' optimization neural network is consistent with GA. While the time cost is only 8% of the latter cause the former does not require an objective value assessment for each individual. It is worth noting that in addition to the variance, other physical information can be extracted from the prediction sound field, which can then be used as our optimization objective for the design of the metasurface.

Table 5 Variance of optimal physical parameters

	Initial minimum variance	FEM simulation	MF-CCNN prediction	Time (s)
GA	0.2292	0.2210	0.1870	242.59
Ours		**0.2209**	0.2127	**20.03**

6 Conclusions

In this paper, the scattered acoustic field uniformity optimization problem is studied with the proposed deep learning-based multi-fidelity optimization framework. The multi-fidelity composite convolutional neural network (MF-CCNN) method is proposed to predict the high-dimensional scattered acoustic field distribution of metasurface to achieve higher precision at a lower data cost. This method first predicts the LF outputs and then maps the LF results to HF results. Specifically, a sub-network is constructed to extract the features of the LF predictions to reduce information redundancy, and another two are utilized to learn the linear and nonlinear correlation between them, respectively. In addition, a fully connected neural network named physical parameters' optimization neural network is proposed to optimize the physical parameters with the prediction of MF-CCNN to obtain the approximately minimum variance.

The proposed MF-CCNN is compared with two multi-fidelity neural networks and the single-fidelity network on datasets of different sizes. We also apply the proposed methodology to optimize the scattered acoustic uniformity. Following conclusions can be drawn: (1) the constructed multi-fidelity neural network MF-CCNN could realize a fast and accurate prediction of the high-dimensional scattered acoustic field. (2) The constructed multi-fidelity neural networks MF-CCNN, MF-PCNN, and BFTL-1 could effectively improve the prediction accuracy. Compared with the model based on single-fidelity data, the mean absolute error is reduced by 20% at least. (3) The mean absolute error of the constructed MF-CCNN is 7.5% lower compared to MF-PCNN and BFTL-1. It is demonstrated that the proposed

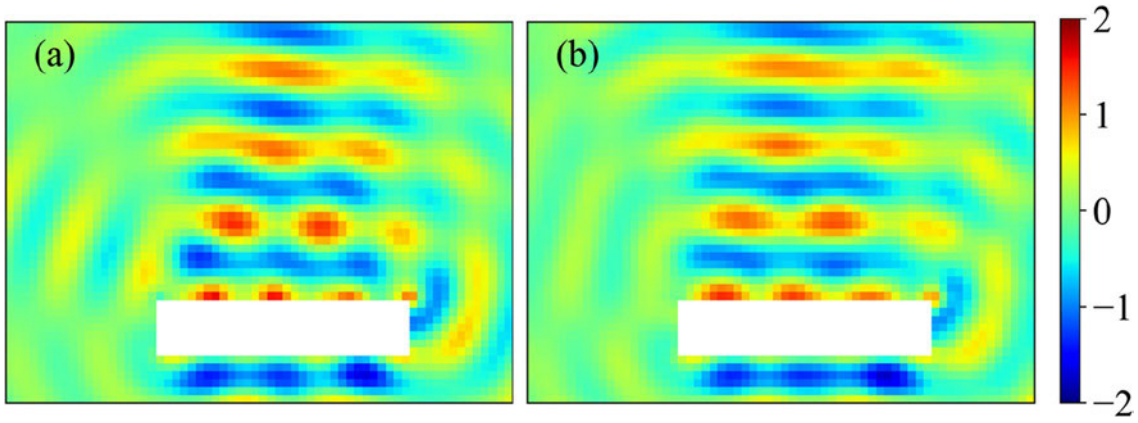

Fig. 23 Obtained optimal scattered acoustic field. **a** FEM simulation, **b** MF-CCNN

scheme can effectively learn linear and nonlinear relationships between HF and LF data. (4) The prediction accuracy of the constructed MF-CCNN gradually increases as the amount of HF data increases, which proves that the proposed method has excellent robustness. (5) The variance after optimization was reduced by 3.62% and the time cost was only 8% of GA, demonstrating the efficiency and accuracy of physical parameters' optimization neural network.

As part of future research, increasing the width and depth of the model and adding residual connections to further improve the prediction accuracy of the model will be investigated. At the same time, incorporating physical constraints [41, 42] will be helpful to reduce the quality requirement of the dataset.

Acknowledgements This research has been partially supported by the National Natural Science Foundation of China (NSFC) under Grant Nos. 52175231, 52105254, 52105256, and the Research Funds of the Maritime Defense Technologies Innovation Nos. JJ2021-719-02, JJ2021-719-03, and JJ2020-719-03-01.

Data availability statement The data that support the findings of this study are available from the corresponding author on reasonable request.

Declarations

Conflict of interest The authors declare that they have no known competing financial interests or personal relationships that could have appeared to influence the work reported in this paper.

References

1. Ma G, Sheng P (2016) Acoustic metamaterials: From local resonances to broad horizons. Sci Adv 2:e1501595
2. Cummer SA, Christensen J, Alù A (2016) Controlling sound with acoustic metamaterials. Nat Rev Mater 1:1–13
3. Xie Y, Wang W, Chen H, Konneker A, Popa B-I, Cummer SA (2014) Wavefront modulation and subwavelength diffractive acoustics with an acoustic metasurface. Nat Commun 5:1–5
4. Zhu Y, Fan X, Liang B, Cheng J, Jing Y (2017) Ultrathin acoustic metasurface-based Schroeder diffuser. Phys Rev X 7:021034
5. Liao G, Wang Z, Luan C, Liu J, Yao X, Fu J (2021) Broadband controllable acoustic focusing and asymmetric focusing by acoustic metamaterials. Smart Mater Struct 30:045021
6. Almeida GDN, Vergara EF, Barbosa LR, Lenzi A, Birch RS (2021) Sound absorption metasurface with symmetrical coiled spaces and micro slit of variable depth. Appl Acoust 183:108312
7. Popa B-I, Zigoneanu L, Cummer SA (2011) Experimental acoustic ground cloak in air. Phys Rev Lett 106:253901
8. Jiang X, Liang B, Cheng JC, Qiu CW (2018) Twisted acoustics: metasurface-enabled multiplexing and demultiplexing. Adv Mater 30:1800257
9. Assouar B, Liang B, Wu Y, Li Y, Cheng J-C, Jing Y (2018) Acoustic metasurfaces. Nat Rev Mater 3:460–472
10. Ma G, Yang M, Xiao S, Yang Z, Sheng P (2014) Acoustic metasurface with hybrid resonances. Nat Mater 13:873–878
11. Cao L, Yang Z, Xu Y, Fan S-W, Zhu Y, Chen Z, Li Y, Assouar B (2020) Flexural wave absorption by lossy gradient elastic metasurface. J Mech Phys Solids 143:104052
12. Yu N, Genevet P, Kats MA, Aieta F, Tetienne J-P, Capasso F, Gaburro Z (2011) Light propagation with phase discontinuities: generalized laws of reflection and refraction. Science 334:333–337
13. Zhao Y, Liu J, Liang B, Cheng J (2020) An ultrathin planar acoustic metasurface diffuser with narrowband uniform reflection. AIP Adv 10:085122
14. Ma G, Fan X, Sheng P, Fink M (2018) Shaping reverberating sound fields with an actively tunable metasurface. Proc Natl Acad Sci 115:6638–6643
15. Gao H, Zhu Y-F, Fan X-D, Liang B, Yang J, Cheng J-C (2017) Non-blind acoustic invisibility by dual layers of homogeneous single-negative media. Sci Rep 7:1–7
16. Miyata K, Noguchi Y, Yamada T, Izui K, Nishiwaki S (2018) Optimum design of a multi-functional acoustic metasurface using topology optimization based on Zwicker's loudness model. Comput Methods Appl Mech Eng 331:116–137
17. Bhosekar A, Ierapetritou M (2018) Advances in surrogate based modeling, feasibility analysis, and optimization: a review. Comput Chem Eng 108:250–267
18. Jin X, Cheng P, Chen W-L, Li H (2018) Prediction model of velocity field around circular cylinder over various Reynolds numbers by fusion convolutional neural networks based on pressure on the cylinder. Phys Fluids 30:047105
19. Bhatnagar S, Afshar Y, Pan S, Duraisamy K, Kaushik S (2019) Prediction of aerodynamic flow fields using convolutional neural networks. Comput Mech 64:525–545
20. Rüttgers M, Koh S-R, Jitsev J, Schröder W, Lintermann A (2020) Prediction of acoustic fields using a lattice-Boltzmann method and deep learning. International Conference on High Performance Computing, Springer, pp 81–101
21. Tian J, Qi C, Sun Y, Yaseen ZM, Pham BT (2021) Permeability prediction of porous media using a combination of computational fluid dynamics and hybrid machine learning methods. Eng Comput 37:3455–3471
22. Liang L, Liu M, Martin C, Sun W (2018) A deep learning approach to estimate stress distribution: a fast and accurate surrogate of finite-element analysis. J R Soc Interface 15:20170844
23. Nie Z, Jiang H, Kara LB (2020) Stress field prediction in cantilevered structures using convolutional neural networks. J Comput Inf Sci Eng 20:011002
24. Guo X, Li W, Iorio F (2016), Convolutional neural networks for steady flow approximation. In: Proceedings of the 22nd ACM SIGKDD International Conference on knowledge discovery and data mining, pp 481–490.
25. Sekar V, Jiang Q, Shu C, Khoo BC (2019) Fast flow field prediction over airfoils using deep learning approach. Phys Fluids 31:057103
26. Kim B, Azevedo VC, Thuerey N, Kim T, Gross M, Solenthaler B (2019) Deep fluids: a generative network for parameterized fluid simulations. Comput Graph Forum 38:59–70
27. Wu H, Liu X, An W, Chen S, Lyu H (2020) A deep learning approach for efficiently and accurately evaluating the flow field of supercritical airfoils. Comput Fluids 198:104393
28. Fan Z, Vineet V, Gamper H, Raghuvanshi N (2020), Fast acoustic scattering using convolutional neural networks. In: ICASSP 2020–2020 IEEE International Conference on Acoustics, Speech and Signal Processing (ICASSP), IEEE, 2020, pp 171–175
29. Donda K, Zhu Y, Merkel A, Fan S-W, Cao L, Wan S, Assouar B (2021) Ultrathin acoustic absorbing metasurface based on deep learning approach. Smart Mater Struct 30:085003
30. Zhao T, Li Y, Zuo L, Zhang K (2021) Machine-learning optimized method for regional control of sound fields. Extreme Mech Lett 45:101297

31. Nansha G, Mou W, Baozhu C (2022) Deep auto-encoder network in predictive design of Helmholtz resonator: on-demand prediction of sound absorption peak. Appl Acoust 191:108680
32. Liao Z, Wang Y, Gao L, Wang Z-P (2022) Deep-learning-based isogeometric inverse design for tetra-chiral auxetics. Compos Struct 280:114808
33. Zhou K, Tang J (2021) Efficient characterization of dynamic response variation using multi-fidelity data fusion through composite neural network. Eng Struct 232:111878
34. De S, Britton J, Reynolds M, Skinner R, Jansen K, Doostan A (2020) On transfer learning of neural networks using bi-fidelity data for uncertainty propagation. Int J Uncertain Quant 10:543–573
35. Liu J, Yi J, Zhou Q, Cheng Y (2022) A sequential multi-fidelity surrogate model-assisted contour prediction method for engineering problems with expensive simulations. Eng Comput 38:31–49
36. Liu D, Wang Y (2019) Multi-fidelity physics-constrained neural network and its application in materials modeling. J Mech Des 141:121403
37. Meng X, Karniadakis GE (2020) A composite neural network that learns from multi-fidelity data: Application to function approximation and inverse PDE problems. J Comput Phys 401:109020
38. Zhang X, Xie F, Ji T, Zhu Z, Zheng Y (2021) Multi-fidelity deep neural network surrogate model for aerodynamic shape optimization. Comput Methods Appl Mech Eng 373:113485
39. Aieta F, Kabiri A, Genevet P, Yu N, Kats MA, Gaburro Z, Capasso F (2012) Reflection and refraction of light from metasurfaces with phase discontinuities. J Nanophotonics 6:063532
40. Kennedy MC, O'Hagan A (2000) Predicting the output from a complex computer code when fast approximations are available. Biometrika 87:1–13
41. Karniadakis GE, Kevrekidis IG, Lu L, Perdikaris P, Wang S, Yang L (2021) Physics-informed machine learning. Nat Rev Phys 3:422–440
42. Raissi M, Perdikaris P, Karniadakis GE (2019) Physics-informed neural networks: a deep learning framework for solving forward and inverse problems involving nonlinear partial differential equations. J Comput Phys 378:686–707